



Dual-optimization strategy engineered Ti-based metal-organic framework with Fe active sites for highly-selective CO₂ photoreduction to formic acid

Xiaoyu He^{a,1}, Xutao Gao^{b,1}, Xiao Chen^c, Shen Hu^a, Fangchang Tan^d, Yujie Xiong^e, Ran Long^e, Min Liu^a, Edmund C.M. Tse^b, Fei Wei^c, Hong Yang^{f,*}, Jungang Hou^{a,*}, Chunshan Song^{a,g,**}, Xinwen Guo^{a,*}

^a State Key Laboratory of Fine Chemicals, PSU-DUT Joint Center for Energy Research, School of Chemical Engineering, Dalian University of Technology, Dalian 116024, China

^b Department of Chemistry, CAS-HKU Joint Laboratory on New Materials, University of Hong Kong, Hong Kong Special Administrative Region of China

^c Beijing Key Laboratory of Green Chemical Reaction Engineering and Technology, Department of Chemical Engineering, Tsinghua University, Beijing 100084, China

^d Division of Glycoscience, Department of Chemistry, School of Engineering Sciences in Chemistry, Biotechnology and Health, KTH Royal Institute of Technology, AlbaNova University Centre, SE-10691 Stockholm, Sweden

^e Hefei National Laboratory for Physical Sciences at the Microscale, Frontiers Science Center for Planetary Exploration and Emerging Technologies, School of Chemistry and Materials Science, National Synchrotron Radiation Laboratory, University of Science and Technology of China, Hefei 230026, China

^f School of Engineering, The University of Western Australia, Perth, WA 6009, Australia

^g Department of Chemistry, Faculty of Science, the Chinese University of Hong Kong, Shatin, Hong Kong Special Administrative Region of China

ARTICLE INFO

Keywords:

Carbon dioxide reduction
Metal-organic frameworks
Visible-light driven photocatalysis
Atomically dispersed Fe sites
High selectivity

ABSTRACT

Increasing CO₂ conversion efficiency over metal-organic framework (MOF) based photocatalysts is of great significance to promote the carbon capture and utilization. In this work, a dual-benefit design strategy is deployed in the synthesis of a new two-dimensional Fe/Ti-BPDC MOF photocatalyst with atomically dispersed Fe sites. This catalyst demonstrated an excellent catalytic performance in the visible-light-driven CO₂ conversion to HCOOH, achieving a high yield of 703.9 μmol g⁻¹ h⁻¹ at a selectivity greater than 99.7%. This is attributed to the ‘dual-optimization’ achieved by this catalyst to sustain the supply of photogenerated electrons and to effectively activate CO₂. Specifically, the Fe/Ti-BPDC catalyst provides a high proportion of effective photogenerated electrons for the CO₂ photocatalysis process via a unique electron transfer mechanism. Meanwhile, the strong O/Fe affinity between CO₂ and atomically dispersed Fe active sites not only enables a fast CO₂ activation, but also dictates the intermediate reaction pathways towards high HCOOH selectivity.

1. Introduction

The drastically increased CO₂ emission attributed to the combustion of fossil fuels worldwide impacts the Earth’s climatic conditions in an unprecedented fashion [1–4]. The global awareness of the need for carbon neutrality drives research towards carbon cycling based on CO₂ capture, utilization, and storage technologies [5,6]. For CO₂ utilization, artificial photosynthesis is a promising strategy to exploit solar-energy conversion of CO₂ to value-added chemicals and for solar energy storage according to bionic principle [7–10]. However, conventional photocatalysts, e.g. homogeneous organic compounds [11,12], inorganic

semiconductors [13–15], and polymeric carbon nitrides [16–19], are usually associated with poor selectivity, because of their complex and uncontrollable active sites causing simultaneous occurrence of multiple reaction pathways [20]. In this context, metal-organic frameworks (MOFs) composed of flexible metal centers and organic ligands present a more promising platform for solar-driven CO₂ conversion [21–25]. The periodically repetitive and well-defined structure provides an opportunity for constructing single-type active sites with uniform microenvironment. This then allows for precise control of catalytic selectivity [26–30]. However, at present, the photocatalytic activity of MOFs is plagued by low effective photoelectrons due to fast electron-hole

* Corresponding authors.

** Corresponding author at: State Key Laboratory of Fine Chemicals, PSU-DUT Joint Center for Energy Research, School of Chemical Engineering, Dalian University of Technology, Dalian 116024, China.

E-mail addresses: hong.yang@uwa.edu.au (H. Yang), jhou@dlut.edu.cn (J. Hou), ChunshanSong@cuhk.edu.hk (C. Song), guoxw@dlut.edu.cn (X. Guo).

¹ These authors contributed equally to this work.

recombination and lack of exposure of active sites.

Fundamentally, the effectiveness of MOF catalysts in supporting CO₂ photoreduction is dictated by two critical aspects, its ability to supply and sustain photogenerated electrons and its effectiveness to activate CO₂ reactant [31,32]. Many studies have been carried out in the past decades aimed at improving photocatalytic performance of MOFs through the optimization of one of these two aspects. To ensure sufficient supply of effective photogenerated electrons, there are two general approaches [33–37]. One is to enhance the light-harvesting capacity of MOFs by, e.g., introducing 2-aminoterephthalic acid ligands with wide photo-response range [33]. Another approach is based on inhibiting electron-hole recombination [38,39]. This is typically done by exploiting a ligand-to-metal charge transfer (LMCT) effect produced with appropriate selection of ligands and clusters for MOFs [34]. LMCT is shown to inhibit recombination of electrons and holes by effectively separating them in physical spaces [35]. On the other aspect of optimizing CO₂ activation, most research is focused on increasing the accessibility of active sites on MOFs to reactants [40–42]. This is typically achieved by designing defects [40] or introducing new active sites [41]. However, a photocatalytic process typically involves complex multi-step chain reactions. Isolated optimization of either aspect could only result in incremental improvement as often observed.

Recently, it was discovered that when a metal with appropriate redox potential is coordinated with the chelating ligands in a MOF, a new energy level could be created in the forbidden band [43]. This means that the introduction of metal onto a MOF already with LMCT effect is feasible to design a unique band structure to support further electron transfer and thus increase the number of effective photogenerated electrons. In addition, if the metal selection could also take into consideration of its affinity for CO₂ and intermediates, it could also accelerate the CO₂ activation and improve the reaction selectivity.

Aimed at achieving ‘dual-optimization’ on photogenerated electron transfer and on CO₂ activation, this work designed and synthesized a novel two-dimensional Ti-MOF-based photocatalyst following the Scheme 1. The catalyst, named Fe/Ti-BPDC, has a formula FeTi₈O₁₂(BPDC)₄(OH)₃(H₂O) where BPDC represents 2,2'-bipyridine-5,5'-dicarboxylic acid. Fe/Ti-BPDC showed excellent photocatalytic performance in CO₂ conversion to HCOOH under visible light. This paper unveiled the electron transfer and CO₂ photoreduction mechanisms underpin the excellent photocatalytic activity of this catalyst.

2. Experimental section

2.1. Materials

All the chemicals were used as received without further purification. The tetraethyl titanate, 2,2'-bipyridine-5,5'-dicarboxylic acid (H₂BPDC), FeCl₃·6H₂O, NiCl₂·6H₂O and CoCl₂·6H₂O were purchased from Aladdin Company. The acetic acid, *N,N*-dimethylformamide (DMF), triethanolamine (TEOA), acetonitrile (MeCN) and ethanol were purchased from Tianjin Damao Chemical Reagent Factory. The Nafion was purchased from Sigma-Aldrich. Deionized water was used throughout this study.

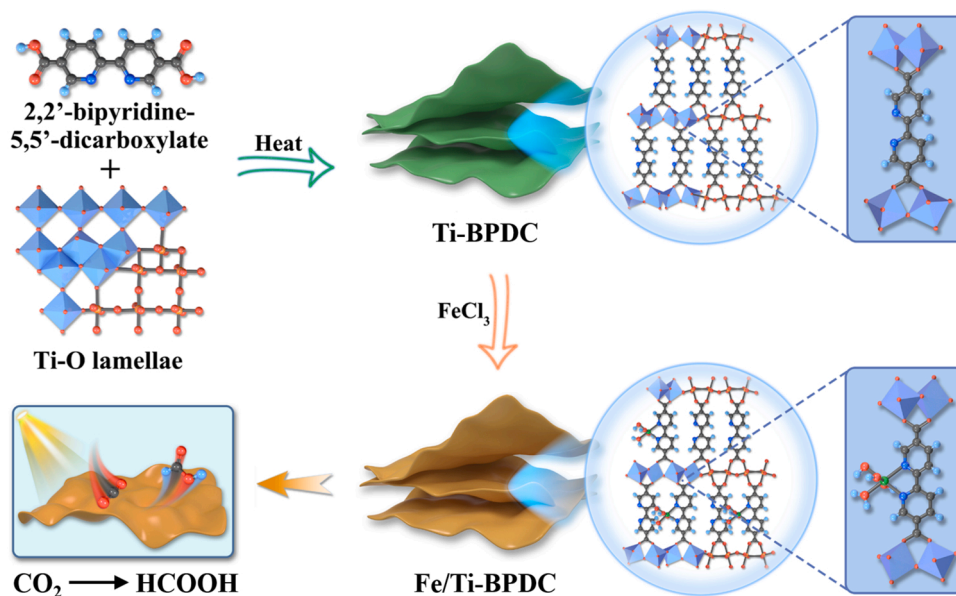
2.2. Synthesis of catalysts

2.2.1. Synthesis of Ti-BPDC

Ti-BPDC is synthesized using a simple one-pot solvothermal method. In a 100 mL beaker, H₂BPDC (100 mg, 0.41 mmol) is dissolved in a mixed solution of DMF (30.0 mL) and acetic acid (1.0 mL) and sonicated for 10 min, before adding tetraethyl titanate (0.13 mL, 0.624 mmol). After 15 min of further sonication, the solution is transferred in a 100 mL Teflon-lined stainless-steel container and maintained at 150 °C for 72 h. The solid product is then collected, washed for several times with DMF and methanol separately, and dried in a vacuum oven at 60 °C for 12 h. The final product is Ti-BPDC, a light-green powder. The yield of this synthesis is ~63% based on H₂BPDC.

2.2.2. Synthesis of M/Ti-BPDC (M=Fe, Co, Ni)

Ti-BPDC (100 mg) is dispersed in 7.50 mL of deionized water and sonicated for 30 min to form a suspension. FeCl₃ solution (9.00 mL, 20 mM, pH=1) is then dropped into the suspension and stirred at 50 °C for 24 h, while maintaining the suspension solution at pH=1. The solid product is recovered by centrifugation, washed with deionized water and ethanol for 5 times, and dried in a vacuum oven at 60 °C for 12 h. The final light-yellow product is Fe/Ti-BPDC. In addition, Fe/Ti-BPDC-0.5 and Fe/Ti-BPDC-0.1 are synthesized using reduced amount of FeCl₃ solution of 2.03 mL and 0.41 mL, respectively while keeping the total amount of solvent unchanged. Co/Ti-BPDC and Ni/Ti-BPDC are synthesized following the same procedure as that of Fe/Ti-BPDC, except of using 9.00 mL of CoCl₂ and NiCl₂ solution (20 mM), respectively,



Scheme 1. Synthesis of the two-dimensional Fe/Ti-BPDC with the atomically dispersed Fe sites for visible-light-driven CO₂ conversion. C, N, O, H, Ti and Fe atoms are colored in grey, dark-blue, red, light-blue, orange and green, respectively.

instead of FeCl_3 solution.

2.2.3. Synthesis of Fe/ H_2 BPDC

The synthesis procedure of Fe/ H_2 BPDC is very similar to that of Fe/Ti-BPDC. H_2 BPDC (100 mg) is dispersed in 10.00 mL of FeCl_3 solution (20 mM, pH=1) and stirred at 50 °C for 24 h, while maintaining the suspension solution at pH=1. The solid product is recovered by centrifugation, washed with deionized water and ethanol for 5 times, and dried in a vacuum oven at 60 °C for 12 h. FT-IR (cm^{-1}): $\nu = 3103$ (w), 3065 (w), 2955 (w), 2827 (w), 2655 (w), 2546 (w), 1676 (vs), 1606 (s), 1575 (m), 1471 (w), 1423 (s), 1370 (m), 1300 (s), 1280 (s), 1247 (s), 1142 (m), 1125 (m), 1055 (m), 1024 (m), 997 (w), 931 (s), 865 (s), 815 (m), 763 (vs), 721 (vw), 690 (m), 645 (m), 558 (m), 545 (m). Anal. Calc.: C, 39.67; H, 1.93; N, 7.71. Found: C, 39.40; H, 2.08; N, 7.63.

2.3. Characterizations

Powder XRD patterns are recorded on a Rigaku SmartLab 9 kW diffractometer, using $\text{Cu K}\alpha$ radiation at 4° min^{-1} scanning rate and a step size of 0.02° . TEM images are taken on a HT7700 EXALENS (Hitachi) and with an acceleration voltage of 300 kV. SEM images are obtained using a SU8220 instruments (Hitachi) with an acceleration voltage of 5 kV. AFM images are taken with a Nanowizard Ultra Speed & inVia Raman (Bruker) and height profiles of the nanostructures are acquired with a JPKSPM Data Processing software. The iDPC-STEM images are obtained under a Cs-corrected STEM (FEI Titan Cubed Themis G2 300) at 300 kV with a convergence semi-angle of 10 mrad. Elemental analysis is carried out with a Vario EL cube instrument (Elementar). ICP-AES data are obtained with Optima 2000dv (Perkinelmer). Thermogravimetric curves are obtained on a SDT Q600 (TA Instruments) from 298 to 1073 K in air at a heating rate of 5 K min^{-1} . XPS measurements are performed on an ESCALAB XI+ spectrometer (Thermo Scientific) with a monochromatic Al $\text{K}\alpha$ X-ray source. X-ray absorption spectroscopy (XAS) spectra of Fe K-edge are collected at BL07A1 beamline of National Synchrotron Radiation Research Center. The data are collected in fluorescence mode using a Lytle detector. The ^{57}Fe Mössbauer spectra are recorded on a Topologic 500 A spectrometer and a proportional counter at 298 K and 77 K. ^{57}Co (Rh) moving in a constant acceleration mode is used as a radioactive source. The analysis of the spectra is conducted assuming a Lorentzian line shape for computer folding and fitting. Attenuated total reflection investigations are performed using a Fourier transform infrared (FT-IR) spectrometer (Nicolet iS50, Thermo Scientific) equipped with a DTGS detector. ^{13}C NMR measurement is carried out using Avance II 400 (Bruker). The NMR spectra are recorded at acquisition time of 1.1 s ca. 27600 times integration. EPR spectra are obtained using an E500 spectrometer (Bruker) at 77 K. Photoluminescence spectroscopy is acquired with a steady state fluorescence and phosphorescence spectrometer (FLS1000, Edinburgh) at an excitation wavelength of 325 nm. UV-Vis DRS experiments are performed using a JASCO V-550 spectrometer. The fs-TA spectra are measured by optical femtosecond pump-probe spectroscopy. The output of a mode-locked Ti: sapphire amplified laser system (Spitfire Ace, Spectra-Physics) with wavelength 800 nm, pulse width 35fs, repetition rate 1 kHz. The *in-situ* SERS is performed using a confocal Raman system (WITTEC alpha300 R) using a 633 nm He-Ne laser as the excitation source.

2.4. Photocatalytic reaction

CO_2 photoreduction is conducted in a 46 mL home-made quartz reactor at 298 K with a circulation cooling system. Visible light is provided by a 300 W Xe lamp (PLS-SXE300C, Beijing Perfectlight Co. Ltd., China) coupled to a UV cutoff filter (420–760 nm). The photocatalyst (5 mg) is dispersed in 6 mL of solution containing 3 mL of acetonitrile (MeCN), 2.5 mL of deionized water (H_2O) and 0.5 mL of triethanolamine (TEOA). The mixture is subjected to ultrasonication for 20 min,

purged with CO_2 (99.999%) for 30 min to remove the dissolved O_2 , and then sealed. The produced gases in the headspace are analyzed by a gas chromatograph (FuLi GC-9790) equipped with connection of a TCD detector and an FID detector with methane reforming furnace (carbon molecular sieve column). The HCOO^- in the liquid phase is analyzed using an ion chromatograph (DIONEX ICS-5000, Thermo Scientific) equipped with CD detector, IonPac AS11-HC column and IonPac AG11-HC guard column. 3.0 mM KOH is used as eluent with the flow rate of 1.0 mL/min. The reaction is repeated three times with different batches of synthesized catalysts to provide more reliable data. The isotope labelled products are analyzed using nuclear magnetic resonance spectrometer (Varian DLG400) with $^{13}\text{CO}_2$ as the feeding gas.

2.5. Photoelectrochemical measurement

Photoelectrochemical tests are conducted with an CHI760E electrochemical workstation (Chenhua, China) in a three-electrode system, using a Pt plate as the counter electrode and Ag/AgCl electrode as the reference electrode. The working electrode is fluorine-tin oxide (FTO) glass ($1 \times 1 \text{ cm}$) coated with sample (the slurry was made of 5 mg of sample dispersed in 0.9 mL of ethanol and 0.1 mL nafion). A 0.2 M Na_2SO_4 solution is used as the electrolyte solution and a 300 W Xe lamp ($420 \text{ nm} < \lambda < 760 \text{ nm}$) as the light source. The Mott-Schottky plots are measured at 500, 1000 and 1500 Hz, respectively.

2.6. In-situ surface-enhanced Raman spectroscopy

The *in-situ* surface-enhanced Raman spectroscopy (SERS) measurements are carried out using a confocal Raman microscope (WITTEC alpha300 R) in a home-made one-compartment 3-electrode spectroelectro-chemical cell. A laser of 633 nm wavelength is used as the excitation source without attenuation by a filter. The grating is calibrated before each set of measurements using the first order peak and the Si lattice peak at 520.7 cm^{-1} of a Si wafer reference sample. The measurements are conducted in a home-made one-compartment 3-electrode spectroelectro-chemical cell made from high-density polyethylene. For each experiment, the laser is focused on the catalyst surface and a $10 \times$ working distance objective lens is employed to collect data. Each SERS spectrum is recorded from 0 to 2200 cm^{-1} with ten accumulations over an acquisition time of 10 s. In the SERS test, a 420 nm LED lamp is used as the excitation light source of photocatalysis, and the surface information of the sample is collected after illumination for different times. In addition, the reproducibility of the spectral signal changes is verified with three duplicate experiments.

2.7. Density functional theory (DFT) calculations

The crystal structures of Ti-BPDC and Fe/Ti-BPDC are optimized by spin-polarized density functional theory (DFT) calculations using the Vienna ab initio simulation package (VASP) [44]. Projector augmented wave (PAW) potentials were implemented with a planewave cutoff energy of 450 eV [45,46]. The generalized gradient approximation (GGA) functional of Perdew-Burke-Ernzerhof (PBE) functional is applied as the exchange-correlation functional [47]. The lattice parameters and all atoms are allowed to relax during geometrical optimization. To better describe the localized d-electrons of Ti and Fe in MOF, the DFT+U approach is utilized with $U_{\text{Ti}} = 3.0$ and $U_{\text{Fe}} = 3.0$, respectively [48]. The grimme's semiempirical DFT-D3 dispersion correction is utilized to describe the van der Waals (vdW) interactions [49]. The convergence criteria of electronic energies and atomic forces for all calculations are 10^{-5} eV and 0.03 eV/\AA . A gamma-centered $4 \times 4 \times 4$ k-points are applied for the MOF structures.

For free energy calculations of visible-light driven CO_2 reduction, the essential clusters of MOF structures are extracted into computationally cost-effective small fragments. The free energy calculations are performed using B3LYP DFT functionals [50]. Basis sets of def2-SVP are

adopted for all atoms in the complexes [51]. Frequency calculations have been carried out at the same computational level. D3 dispersion correction developed by Grimme is included for weak interactions [52]. All of the free-energy computation steps are performed using the Gaussian 16 program package [52].

3. Results and discussion

3.1. Morphology and framework of Fe/Ti-BPDC

Ti-BPDC is grown from H₂BPDC and tetraethyl titanate precursors through simple solvothermal method. Then atomically dispersed Fe is reasonably introduced into Ti-BPDC through coordinatively binding to ligands, resulting in Fe/Ti-BPDC (see **Experimental Section**). The irregularly shaped lamellar morphology is observed for Fe/Ti-BPDC (Fig. 1a), exhibiting uniform thickness (height in Fig. 1b) of ~6 nm. The as-prepared Fe/Ti-BPDC consists of well-dispersed individual lamella.

To understand the structure of Fe/Ti-BPDC, the Ti-BPDC framework needs to be decoded first. As revealed by the X-ray diffraction (XRD) pattern shown in Fig. 2a, Ti-BPDC is of high crystallinity. The integrated differential phase contrast scanning transmission electron microscopy (iDPC-STEM) image (Fig. 2b) taken perpendicular to the stacking direction shows periodical arrangements of Ti and O atoms forming the Ti-O layers. And the iDPC-STEM images (Fig. 2c, Fig. S1) taken parallel to the basal plane reveals parallel to each other Ti-O layers of constant spacing of 1.51 nm connected by ligands (highlighted in yellow). Based on the atomic arrangements unveiled and take into the consideration of cluster and ligand connectivity, several possible framework structures for Ti-BPDC are conceived. *Materials Studio* (2017) is used to build and optimize these possible framework model [53]. The optimized model (Table S1) whose simulated patterns match well with the experimental PXRD patterns is selected. Pawley refinement is then performed to optimize the final unit cell parameters (Fig. 2a, Table S2). The detailed structure modeling procedures are provided in the supplementary information. Figs. 2d and 2e depict the framework structure viewed in *a-c* plane and along *c*-axis, respectively. Each Ti atom is connected to six O atoms to form Ti-oxo clusters, of which two O atoms come from the ligands H₂BPDC and four O atoms come from the Ti-O layers. The chemical formula for Ti-BPDC is derived as Ti₈O₁₂(C₁₂H₆N₂O₄)₄, which is further confirmed by elemental analysis, inductively coupled plasma atomic emission spectrometry (ICP-AES) and thermogravimetric analysis (Table S3).

In this work, Fe is anchored on the pre-synthesized Ti-BPDC MOF skeleton. The coordination of Fe with bipyridine-N, the MOF ligand, is vindicated by the N 1s XPS spectra (Fig. S2). It shows the pyridinic-N peak in Fe/Ti-BPDC shifts to a higher binding energy of 399.3 eV from the 398.8 eV of Ti-BPDC, indicating strong interaction between Fe and

pyridinic-N. ICP-AES analysis shows that 2.88 wt% Fe is in Fe/Ti-BPDC by metalation. However, it is seen that there is still a high number of pyridinic-N uncoordinated Fe in Fe/Ti-BPDC from the N 1s XPS spectra. This indicates that the Fe content may have reached the saturation in the MOF. It is demonstrated by Fig. S3 where the Fe content remains unchanged after reaching ~2.9 wt% in the MOF synthesized with the increasing of FeCl₃ dosage. This is likely due to the steric hindrance of the MOF skeleton preventing more Fe loading onto the MOF. XRD combined with iDPC-STEM (Figs. S4–5) shows that the introduction of Fe does not change the framework structure of Ti-BPDC and the local structure of Ti. Moreover, the Ti-O layers arranged orderly in parallel provide strong structural stability, endowing excellent thermal and solution stability of Fe/Ti-BPDC (Figs. S6–7). More importantly, the comparison of Ti 2p XPS spectra of Ti-BPDC and Fe/Ti-BPDC (Fig. S8) shows that the introduction of Fe does not alter the electronic structure of Ti.

To confirm the valence state of Fe and its coordination environment in Fe/Ti-BPDC, the catalyst is analyzed by X-ray absorption spectroscopy (XAS), X-ray photoelectron spectroscopy (XPS) and Mössbauer spectroscopy. As shown in the X-ray absorption near edge spectra (XANES, Fig. 3a), the Fe species in Fe/Ti-BPDC has an edge energy of 7125.9 eV, which is very close to those of Fe₂O₃ (7125.7 eV) and Fe-MFI (7125.8 eV), confirming the presence of Fe(III). The oxidation state of Fe is also verified by Fe 2p XPS (Fig. S9) [54]. From the XANES spectra, the pre-edge energy and calculated area of Fe/Ti-BPDC, Fe₂O₃ and Fe-MFI are summarized in Table S4. As seen, the pre-edge area of Fe/Ti-BPDC (5.6×10^{-2} eV) is very close to Fe₂O₃ (5.2×10^{-2} eV) but much smaller than that of Fe-MFI (5.2×10^{-2} eV). Known that Fe₂O₃ has an octahedral (O_h) coordination geometry and Fe-MFI has a tetrahedral (Td) coordination geometry, the result indicates that Fe has six-coordination in Fe/Ti-BPDC. Further fitting of the EXAFS spectra suggests that the Fe(III) metal center in Fe/Ti-BPDC is surrounded by 5.4 ± 0.4 N (and O) atoms at a distance of 1.98 ± 0.01 Å (Fig. 3b, Fig. S10, Table S5). Note that EXAFS spectrum alone could not conclusively distinguish N from O in this case. ⁵⁷Fe Mössbauer spectroscopy is also used to probe into the coordination structure of Fe in Fe/Ti-BPDC. The spectra were measured at 298 and 77 K, respectively (details provided in Fig. S11 and Table S6). There is only a signal ascribed to a mononuclear Fe(III) species with a six-coordination, as well as a relaxation signal caused by this Fe species, observed in Fe/Ti-BPDC Mössbauer spectra. This result indicates that there could only be one unique Fe local structure in Fe/Ti-BPDC, which is consistent with the XAFS results.

Taking into consideration of all above, it is concluded that Fe in Fe/Ti-BPDC exists as atomically dispersed Fe(III) in six-coordination with N (and O). Based on this, a number of possible hypothetical skeleton structures are constructed. The density functional theory (DFT) calculation was carried out to determine the final coordination structure of

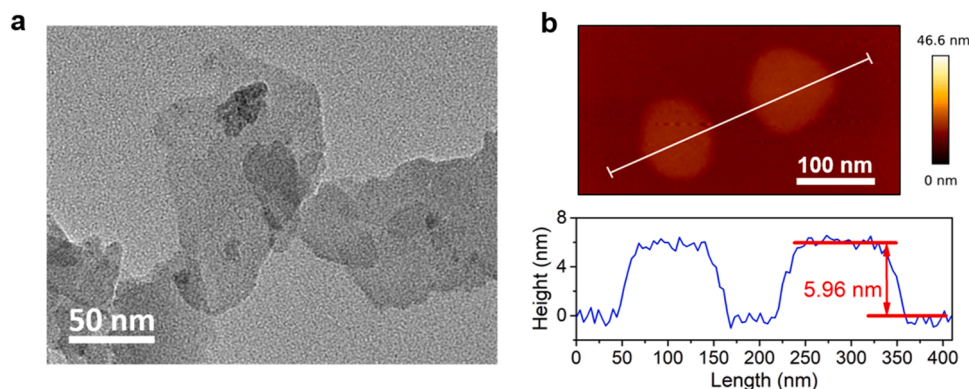


Fig. 1. Morphology of the fabricated Fe/Ti-BPDC. (a) Transmission electron microscope (TEM) image of the lamellae. (b) Atomic force microscope (AFM) image and thickness analysis of lamellae.

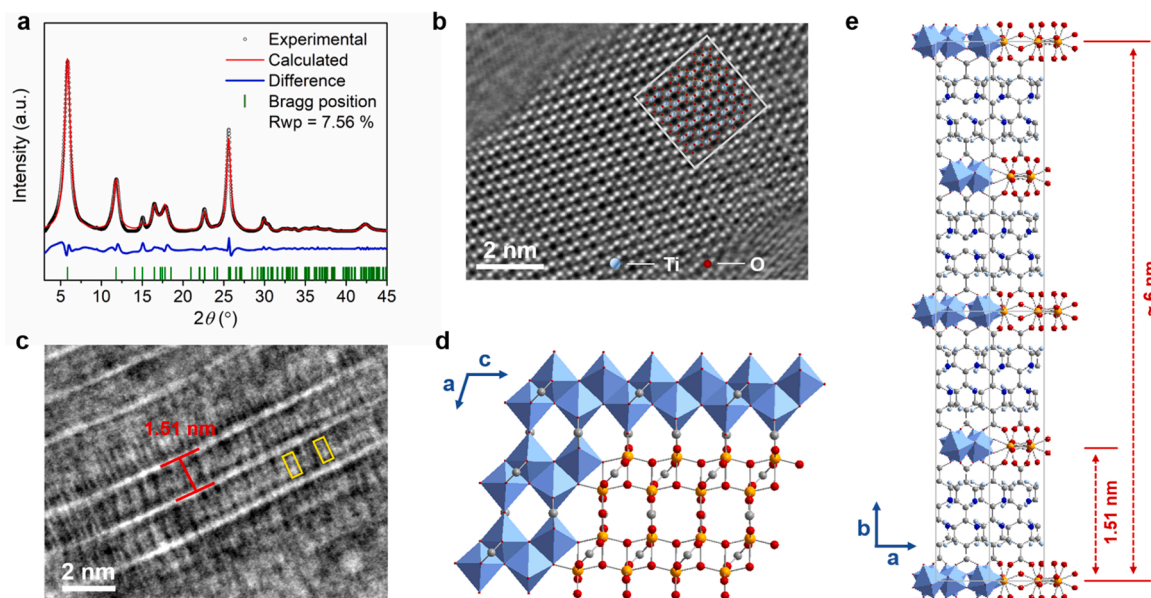


Fig. 2. Determination of framework structure of Ti-BPDC. (a) XRD analysis of Ti-BPDC displaying the experimental pattern (black), refined Pawley fitting (red), difference plot (blue) and Bragg positions (green). The iDPC-STEM images taken along (b) vertical and (c) parallel direction of crystal lamella. Framework structure viewed (d) in *a-c* plane showing Ti-O layers and (e) along *c*-axis. C, N, O, H and Ti atoms are colored in grey, dark-blue, red, light-blue and orange, respectively.

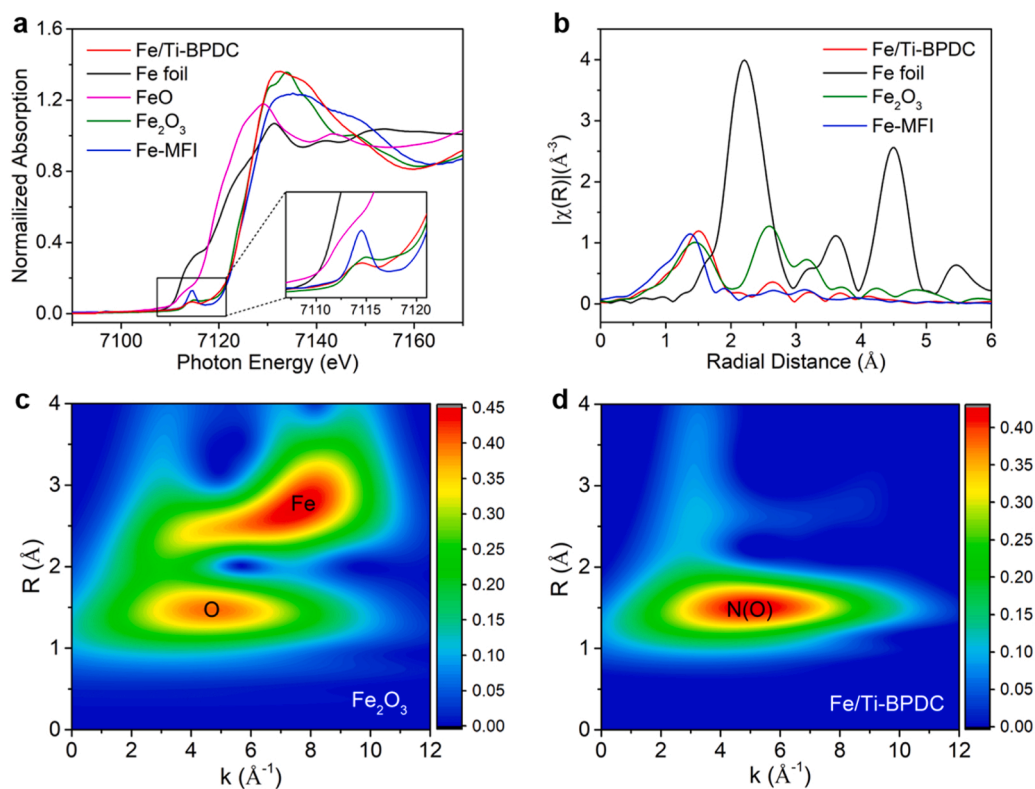


Fig. 3. Structural analysis of Fe sites in Fe/Ti-BPDC. (a) XANES spectra of Fe/Ti-BPDC and various control materials. (b) k^2 -weighted FT magnitudes of the EXAFS spectra over Fe/Ti-BPDC and various control materials. Wavelet analysis of the EXAFS data over (c) Fe₂O₃ and (d) Fe/Ti-BPDC.

Fe. It unveils the only stable structure, Fe-2N-3O-O, for Fe/Ti-BPDC, where Fe connects to two N atoms of a bipyridine ligand and connects externally to the O atoms of three OH⁻ groups and one H₂O molecule. Finally, it is worth noting that both the EXAFS and ⁵⁷Fe Mössbauer analyses also indicate that there are no impurity phases in the synthesized Fe/Ti-BPDC. EXAFS wavelet analysis as shown in Fig. 3c reveals a second-shell peak ($R \sim 2.8$ Å, phase shift uncorrected) for Fe₂O₃, related

to the Fe•••Fe scattering. In contrast as seen in Fig. 3d for Fe/Ti-BPDC, this signal is completely absent, proving there is no Fe₂O₃ impurity in Fe/Ti-BPDC. Similarly, as revealed in ⁵⁷Fe Mössbauer spectra, neither the typical sextet peaks corresponding to α -Fe, FeO and Fe₂O₃, nor the typical singlet peak corresponding to γ -Fe are detected.

3.2. Photocatalytic performance

Fig. 4 shows the results of visible-light-driven CO_2 conversion as determined in a three-phase system. Strikingly, as shown in Fig. 4a, a very high yield of HCOOH, $703.9 \mu\text{mol g}^{-1} \text{h}^{-1}$ on average, is achieved over Fe/Ti-BPDC, corresponding to selectivity up to 99.7%. In addition to HCOOH, only trace amounts of CO and CH_4 and no H_2 are detected (Fig. S12). In contrast, over Ti-BPDC, the HCOOH production rate is only $184.9 \mu\text{mol g}^{-1} \text{h}^{-1}$. Notably that Fe/ H_2 BPDC, in which Fe species are directly chelated by ligands, exhibits very low activity (Figs. S13 and S14). This indicates the important role of MOF skeleton in photocatalysis. The advantage for such catalyst design is further demonstrated by the apparent quantum yield (AQY) measurement results at various wavelengths. The AQY values of Fe/Ti-BPDC at 420 and 450 nm are 7.82% and 6.32%, respectively (Fig. S15). They are much higher than those of Ti-BPDC (1.80% and 1.51%, respectively) and Fe/ H_2 BPDC (0.33% and 0.27%, respectively). In addition, Fig. 4a also shows the effect of Fe-loading in Fe/Ti-BPDC on CO_2 photoreduction. Fe/Ti-BPDC-0.5 and Fe/Ti-BPDC-0.1 are the catalysts in which the Fe-loading in Fe/Ti-BPDC is reduced to one half and one tenth, respectively. As determined by ICP-AES, the true Fe-loading is 1.46 wt% in Fe/Ti-BPDC-0.5 and 0.33 wt% in Fe/Ti-BPDC-0.1. The higher Fe-loading is in the catalyst, the higher production of HCOOH is achieved. This implies that Fe species serve as catalytic centers in this catalyst. Fe/Ti-BPDC still exhibits great catalytic activity after 10 recycling tests (Fig. S16), demonstrating the robustness of this catalyst. Further experimental analysis on the skeleton stability including the morphology of Fe/Ti-BPDC after long-term reactions are provided in Figs. S17–18 and Table S7. Compared to the similar MOF-based catalysts and other catalytic systems reported in recent years [22,27,36,55–80], Fe/Ti-BPDC exhibits a high HCOOH yield within the first tire of all reviewed systems, accompanied by a surprisingly high HCOOH selectivity (Table S8).

To confirm the real conversion of the carbon in CO_2 to HCOOH, a $^{13}\text{CO}_2$ isotope labelling experiment is conducted with Fe/Ti-BPDC (Fig. 4b). Three distinct peaks at 159.3, 160.7 and 164.7 ppm are observed in the ^{13}C NMR of $^{13}\text{CO}_2$ photoreduction product, corresponding to $\text{H}^{13}\text{CO}_2^-$, $^{13}\text{CO}_3^{2-}$ and $\text{H}^{13}\text{COO}^-$, respectively (Fig. S19). In contrast, there is no similar peak with $^{12}\text{CO}_2$ as reaction raw material. This shows that the product is produced only from $^{13}\text{CO}_2$ feed. In addition, a control experiment using N_2 instead of CO_2 as feed also shows no HCOOH and other products (Fig. S20). These prove that the carbon source in the products of CO_2 photoreduction over Fe/Ti-BPDC is completely derived from the CO_2 feed, rather than the organic ligands in the catalyst.

3.3. Electron-transfer mechanism

To reasonably analyze the changes of catalytic performance, the

electron-transfer mechanisms of Ti-BPDC and Fe/Ti-BPDC are studied firstly. Fig. 5 presents evidences for establishing the electron-transfer mechanism in visible-light-driven CO_2 reduction over Ti-BPDC and Fe/Ti-BPDC. Interestingly, it is observed that Fe/Ti-BPDC changes color from yellow to pink after illumination during the CO_2 reduction, indicating valence state change from Fe(III) to Fe(II) (Fig. S21). And when the illumination ends, the catalyst returns to yellow. The quasi *in-situ* electron paramagnetic resonance (EPR) is used to analyze the changes of metal valence states during photocatalysis [81,82]. For Ti-BPDC, a signal at $g = 1.976$ is observed post illumination testing in Ar (Fig. S22). This is ascribed to Ti(III), indicating that photogenerated electrons are captured by Ti-oxo clusters inducing Ti(IV) to Ti(III) transition. Note that this signal diminishes when CO_2 is introduced to the system, suggesting the electrons transfer is now switched from Ti-oxo clusters to CO_2 . In this context, Ti plays the role of active sites in Ti-BPDC. However, for Fe/Ti-BPDC, a completely different electron transfer behavior is observed. As shown in Fig. 5a, a EPR signal at $g = 4.236$ is observed in the dark under Ar, which is typically associated with the mononuclear Fe(III). Obviously, this signal quenches with the illumination in Ar, but recovers with the subsequent introduction of CO_2 . This process reveals electron transfer from Fe(III) to Fe(II) and then to CO_2 . This corresponds perfectly to the changes of catalyst color during the reaction (Fig. S21). This proves that the active sites of Fe/Ti-BPDC are indeed atomically dispersed Fe species. In addition, no change in the valence state of Ti is observed in the Fe/Ti-BPDC EPR during the whole reaction. This seems to suggest that in Fe/Ti-BPDC, Ti only plays the role of electron relay to help transfer photogenerated electrons to Fe sites, but do not store photogenerated electrons.

To explain this phenomenon, the electronic band structures of Ti-BPDC and Fe/Ti-BPDC are constructed firstly based on the results and analysis of a series of photoelectrochemical measurements (Fig. S23). The results reveal that Ti-BPDC and Fe/Ti-BPDC both possess appropriate band structures for solar-driven CO_2 reduction (Fig. 5b) [83,84]. Compared with Ti-BPDC, Fe/Ti-BPDC has a significantly narrower optical band gap. It is also noted that Fe/Ti-BPDC has a second bandgap (1.77 eV), which means there is a new band lower than the conduction-band minimum (CBM) of Ti-BPDC in Fe/Ti-BPDC. This is attributed to the doping level brought by the introduction of atomically dispersed Fe species with low redox potential. The experimental results are verified by DFT calculation. By comparing the electronic band structures (Fig. S24) and the partial density of state distributions (Figs. 5c and 5d) of Ti-BPDC and Fe/Ti-BPDC, it is found that not only the band gap of Fe/Ti-BPDC becomes narrower, it also has a new energy level (III in Fig. 5d) appeared in the forbidden band. This result perfectly matches the electronic band structures derived empirically (Fig. 5b).

The electron transfer behaviors in the photocatalytic process are reasonably speculated by analyzing the charge distribution of each energy band. Figs. 5e and 5f provide the visual presentations of charge

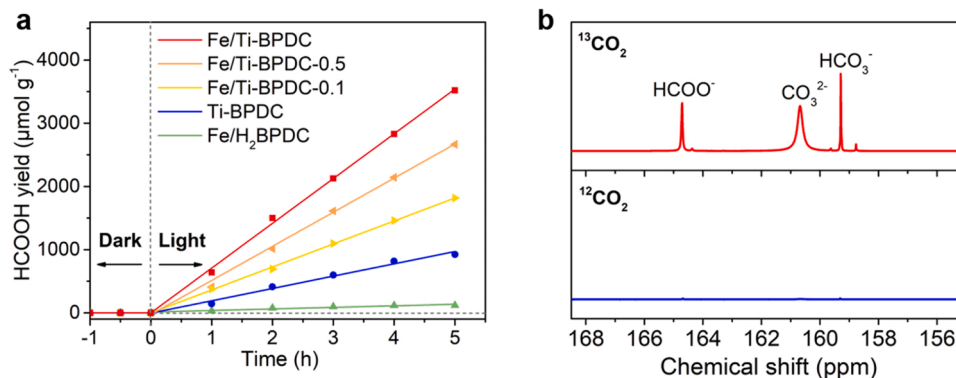


Fig. 4. Photocatalytic performance of CO_2 reduction over Fe/Ti-BPDC. (a) HCOOH production as a function of reaction time under visible-light irradiation (420–760 nm) over catalysts. (b) ^{13}C NMR spectra of products of $^{13}\text{CO}_2$ and $^{12}\text{CO}_2$ photoreduction over Fe/Ti-BPDC.

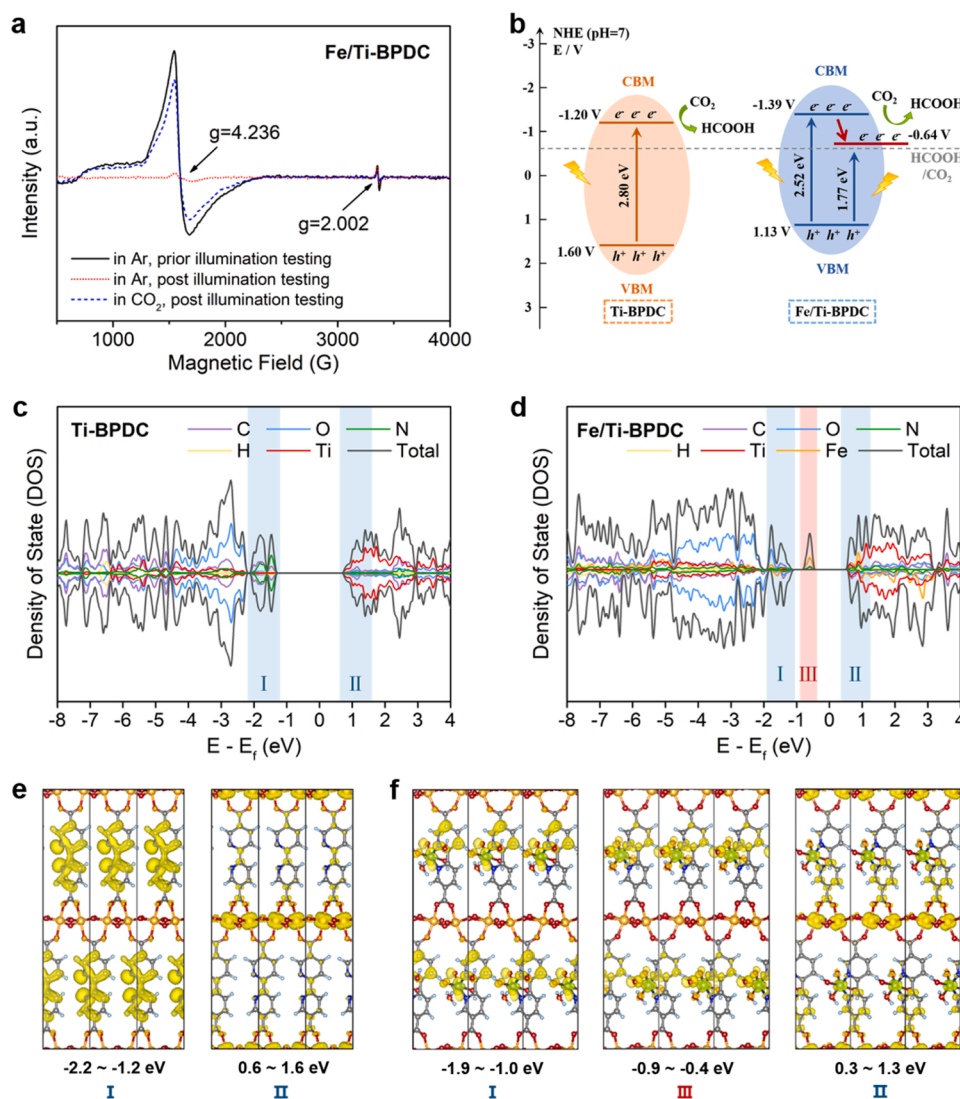


Fig. 5. Proposed electron-transfer mechanism over Ti-BPDC and Fe/Ti-BPDC. (a) Quasi *in-situ* EPR spectra of Fe/Ti-BPDC. (b) The derived electronic band structures of Ti-BPDC and Fe/Ti-BPDC from empirical results. The partial density of state distributions of (c) Ti-BPDC and (d) Fe/Ti-BPDC. Partial charge density maps drawn at 0.02 e/Å³ iso-surface level of (e) valence band (I) and conduction band (II) for Ti-BPDC and (f) valence band (I), conduction band (II) and a new band (III) for Fe/Ti-BPDC. C, N, O, H, Ti and Fe atoms are colored in grey, dark-blue, red, pale-blue, orange and green, respectively.

distributions in Ti-BPDC and Fe/Ti-BPDC, respectively. For both catalysts, their valence-band maximum (VBM) is principally localized on the π -bonding orbitals of the ligands (I in Figs. 5e and 5f), the CBM is principally localized on Ti-oxo clusters (II in Figs. 5e and 5f), and the new band in Fe/Ti-BPDC is mainly originated from the Fe atom and its coordination environment (III in Fig. 5f). Therefore, in both Ti-BPDC and Fe/Ti-BPDC with MOF skeletons, the photogenerated electrons are produced by the visible-light excitation of H₂BPDC ligands during the photocatalytic process. These photogenerated electrons then transfer from the ligands to the Ti-oxo clusters via the LMCT process. The carrier space separation caused by the ligand-cluster skeleton effectively inhibits the rapid recombination of the electrons and holes. In Ti-BPDC, the photogenerated electrons transferring to Ti-oxo clusters reduce Ti (IV) to Ti(III) and empower it to reduce CO₂. However, in Fe/Ti-BPDC, the new energy level produced by the introduction of Fe provides a more stable platform for photogenerated electrons because of its lower potential. Thus, the photogenerated electrons will further transfer to the Fe species and reduced Fe(III) to Fe(II). These are consistent with the color change of catalysts during the experiment and the quasi *in-situ* EPR results above.

Femtosecond transient absorption (fs-TA) spectra provide further evidences for the speculation of the above electron transfer behaviors. The decay curves of Ti-BPDC and Fe/Ti-BPDC are both fitted with a multi-exponential model to analyze the transient charge-separation

kinetics (Figs. S25 and S26, Table S9). There are some similarities between the two catalysts, such as the extremely long-lifetime τ_4 representing the intermediate state with extended electron-hole separation, τ_2 corresponding to the LMCT process [35] and the extremely short-lifetime τ_1 belonging to the conventional semiconductor nature of MOFs [85]. However, it is worth noting that, unlike Ti-BPDC, Fe/Ti-BPDC shows $\tau_3 = 220$ ps, which is deduced to be the electron transfer from LUMO of Ti-oxo cluster to the new lower energy level produced by Fe species after LMCT. In addition, the shorter lifetime and larger proportion of transferred charges in the fitting results imply that Fe/Ti-BPDC should have higher charge separation efficiency.

Empirically as revealed by the transient photocurrent responses (Fig. S27a), Ti-BPDC exhibits a higher photocurrent density than H₂BPDC. Not only so, the Fe-loading in Fe/Ti-BPDC further enhances the photocurrent density than Ti-BPDC. On the other hand, as demonstrated by the photoluminescence spectra (Fig. S27b), compared with H₂BPDC, the formation of Ti-BPDC skeleton enhances the fluorescence quenching which is further enhanced by the Fe-loading in Fe/Ti-BPDC. This verifies the above speculations about electron transfer efficiency that the formation of MOF skeleton is favorable for the transfer of photogenerated electrons through the LMCT process, and the introduction of Fe makes Fe/Ti-BPDC show higher photogenerated electron transfer efficiency due to the unique electronic band structure and the strong driving force of the new energy level. Consequently, in Fe/Ti-BPDC, a higher

proportion of photogenerated electrons are used for active charge transfer rather than electron-hole recombination, which plays a positive role in the catalytic reaction.

Finally, the quenching mechanism of visible-light driven CO_2 reduction over Fe/Ti-BPDC is studied by the photoluminescence spectrometry to delineate the electron transfer behavior on Fe/Ti-BPDC during CO_2 reduction more completely [86]. The liquid-photoluminescence spectra show the CO_2 photoreduction over Fe/Ti-BPDC follows the oxidative quenching mechanism, where the electrons transfer to the active sites precedes the holes quenching by TEOA (Fig. S28).

The following electron-transfer mechanism is established for the visible-light-driven CO_2 conversion over Fe/Ti-BPDC, through both empirical studies and DFT calculations. Essentially, the ligands in the catalyst could be considered as “electron donors”, which can be excited to offer photogenerated electrons to Ti-oxo through the LMCT process. Due to the instability of higher excited state (LUMO of Ti-oxo clusters),

the photogenerated electrons again rapidly migrate to the new and lower energy level created by Fe species and reduce Fe(III) to Fe(II). Then, the holes on ligands are consumed by TEOA, preventing the electron-hole recombination. Finally, the photogenerated electrons are transferred from Fe(II) to CO_2 during CO_2 activation, in which Fe species serve as “mediators”. The atomically dispersed Fe sites provide a strong electron-transfer driving force through the regulation of Fe/Ti-BPDC electronic band structures and significantly enhance the utilization efficiency of photogenerated electrons.

3.4. CO_2 -photoreduction mechanism

To understand the CO_2 -activation mechanism on the active sites, the intermediates formation is studied by the *in-situ* surface-enhanced Raman spectroscopy (SERS) and DFT calculation (Fig. 6) [87,88]. The *in-situ* SERS spectra obtained during CO_2 photoreduction reveal two intermediates for both Fe/Ti-BPDC and Ti-BPDC (Figs. 6a and 6b and

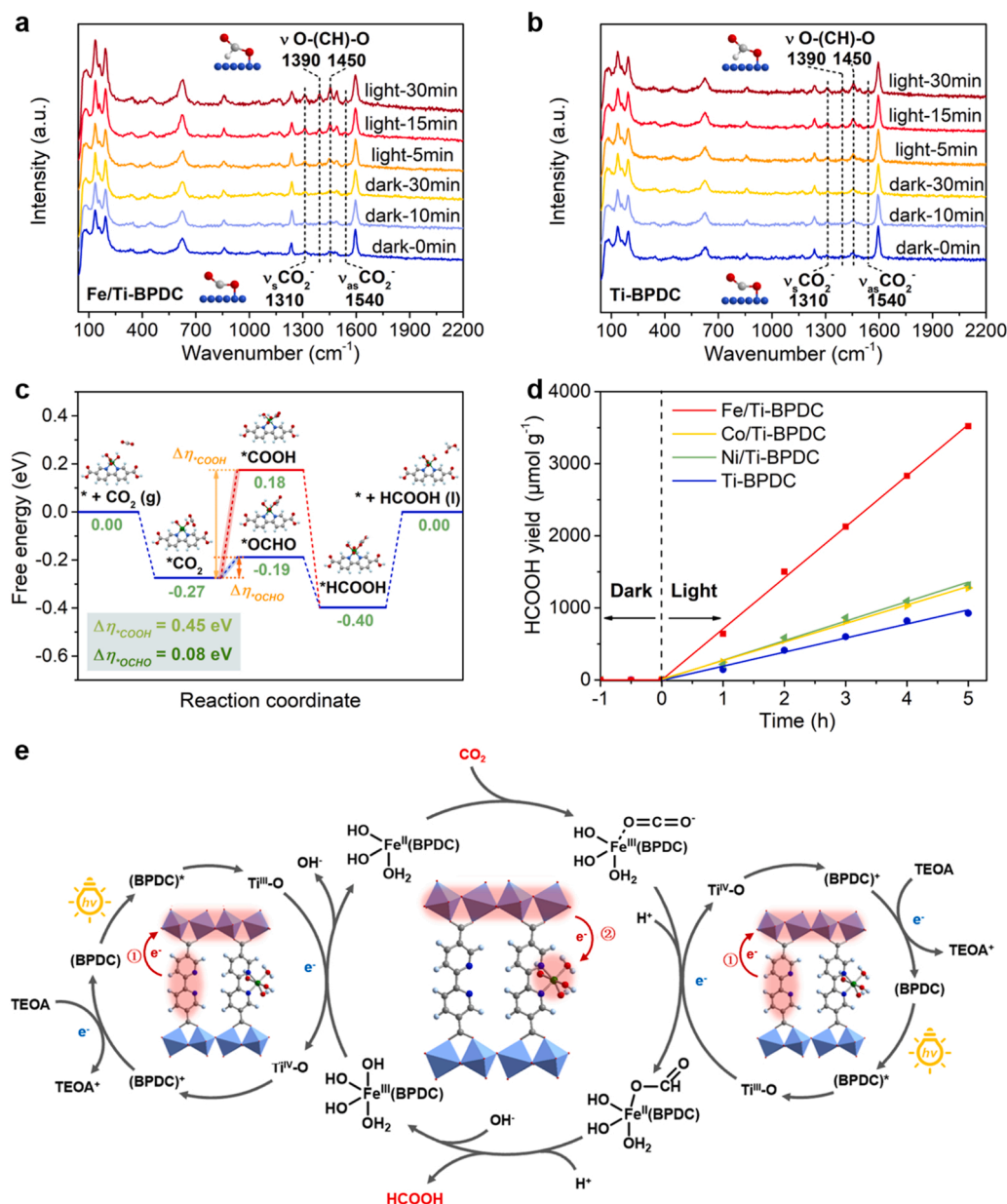


Fig. 6. Proposed reaction mechanism in photocatalytic CO_2 reduction. *In-situ* SERS spectra during CO_2 photoreduction over (a) Fe/Ti-BPDC and (b) Ti-BPDC. (c) Calculated free-energy diagram for CO_2 photocatalytic reduction to HCOOH over Fe/Ti-BPDC at $U = 0.2$ V vs. RHE. (d) HCOOH productivity curves under visible-light irradiation (420–760 nm) over M/Ti-BPDC (M=Fe, Co, Ni) and Ti-BPDC. (e) Proposed photocatalytic mechanism of CO_2 to HCOOH over Fe/Ti-BPDC.

Fig. S29). Firstly, the peaks at 1310 and 1540 cm^{-1} belong to the symmetric stretching vibration ($\nu_{\text{s}}\text{CO}_2$) and asymmetric stretching vibration ($\nu_{\text{as}}\text{CO}_2$) of $^*\text{OCO}^-$, respectively. They represent the CO_2 intermediate, likely produced by CO_2 activation via O on Fe active sites. In addition, the two peaks at 1390 and 1450 cm^{-1} are assigned to the symmetric stretching modes of a protonated intermediate, $^*\text{OCHO}$. Notably, not only no $\nu\text{C}\equiv\text{O}$ signal related to CO generation is observed, the characteristic peaks associated with $^*\text{CO}_2$ and $^*\text{COOH}$ are also absent. The detailed assignments of Raman shifts for reaction intermediates are provided in **Table S10**. These imply that the activation of CO_2 via C on Fe active sites is unfavored. This explains the highly selective visible-light-driven CO_2 conversion to HCOOH on Fe/Ti-BPDC.

The free-energy diagram of CO_2 photoreduction to HCOOH over Fe/Ti-BPDC is derived from DFT calculations (**Fig. 6c**). For the $^*\text{CO}_2$ protonation step, two scenarios associated with $^*\text{OCHO}$ (triggered by O/Fe) intermediate and $^*\text{COOH}$ (triggered by C/Fe) intermediate are considered. As revealed, the $^*\text{CO}_2$ protonation to form $^*\text{OCHO}$ required a much lower activation energy barrier to overcome than to form $^*\text{COOH}$, at 0.08 eV vs. 0.45 eV. Hence, $^*\text{OCHO}$ intermediate would dominate. This also unveils the decisive role played by the strong affinity of O/Fe on the reaction selectivity over Fe/Ti-BPDC.

It should be pointed out that the comparative studies of CO_2 photoreduction to HCOOH are also carried out over other M/Ti-BPDC (M=Co and Ni) catalysts prepared in the same way (**Figs. S30 and S31, Table S11, Fig. 6d**). Notably Co/Ti-BPDC and Ni/Ti-BPDC show a much lower catalytic activity than Fe/Ti-BPDC, although they are still more active than Ti-BPDC. This highlights the important influence of O/M affinity between CO_2 and metals, as the affinity of O/Ni or O/Co is noticeably lower than that of O/Fe [89]. The lower performance of Ti-BPDC is due to insufficient exposure of Ti active sites in Ti-oxo cluster. The relevant DFT calculation results show that the protonation step to $^*\text{HCOOH}$ or $^*\text{OCHO}$ triggered by O/M is associated with a significantly higher activation energy for Co/Ti-BPDC and Ni/Ti-BPDC than for Fe/Ti-BPDC (**Fig. S32**). This further illustrates the important role played by the affinity of O/M (the active site) in the proton-transfer process and CO_2 activation.

Finally, **Fig. 6e** depicts the overall photocatalytic mechanism of CO_2 to HCOOH over Fe/Ti-BPDC. Essentially, electrons are generated by photoexcited ligands and transferred via Ti-oxo clusters to the atomically dispersed Fe active sites, converting Fe(III) to Fe(II). The visible-light driven CO_2 reduction occurs via the following double-electron transfer process. Firstly, CO_2 is adsorbed on Fe active sites, which interact with the O in CO_2 to realize the first electron transfer to form $^*\text{OCO}^-$ intermediate. Then the $^*\text{OCO}^-$ is further protonated to $^*\text{OCHO}$. At the same time, another electron from ligand transfers to the Fe active site. This permits the second electron transfer from Fe active sites to $^*\text{OCHO}$ for its protonation to form $^*\text{HCOOH}$. Finally, the product HCOOH leaves Fe/Ti-BPDC.

4. Conclusions

In this work, a novel high-performance MOF-based photocatalyst, Fe/Ti-BPDC, was designed and synthesized for visible-light-driven CO_2 conversion. The Fe/Ti-BPDC catalyst delivered an excellent yield of 703.9 $\mu\text{mol g}^{-1} \text{h}^{-1}$ and a greater than 99.7% selectivity in CO_2 photoreduction to HCOOH. Essentially, the cooperative coordination between Ti-oxo clusters, chelating ligands, and atomically dispersed Fe active sites enables the Fe/Ti-BPDC catalyst to realize a ‘dual-optimization’ on the sustained supply of photogenerated electrons for catalysis and on the enhanced CO_2 activation. Specifically, the photogenerated electron transfer in Fe/Ti-BPDC occurs via a unique electron transfer mechanism. Firstly, the electrons generated by the excited ligands arrive at the Ti-oxo clusters via a LMCT process in Ti-BPDC MOF. A high proportion of these electrons then transfer again to the new and lower energy band created by Fe-ligand interaction. This mechanism ensures a sustained supply of large numbers of effective photogenerated electrons for

catalysis. At the same time over Fe/Ti-BPDC, the adsorbed CO_2 are activated via its O at the Fe active sites to generate $^*\text{OCO}^-$ and then $^*\text{OCHO}$ intermediates. The $^*\text{OCHO}$ is further protonated to form HCOOH. In this process, the strong O/Fe affinity supported by the atomically dispersed Fe active sites on the catalyst not only plays a decisive role on the reaction selectivity to form HCOOH, but also enables fast CO_2 activation. This study proves the feasibility of this dual-benefit design strategy. The strategy is versatile and of unprecedented significance in creating new MOF-based catalysts for efficient CO_2 photoreduction.

CRedit authorship contribution statement

Xiaoyu He: Conceptualization, Investigation, Methodology, Formal analysis, Validation, Writing – original draft. **Xutao Gao:** Writing – original draft. **Xiao Chen:** Visualization, Writing – review & editing. **Shen Hu:** Investigation, Methodology, Formal analysis. **Fangchang Tan:** Formal analysis, Software, Writing – review & editing. **Yujie Xiong:** Investigation. **Ran Long:** Investigation. **Min Liu:** Supervision, Writing – review & editing. **Edmund C. M. Tse:** Writing – review & editing. **Fei Wei:** Visualization. **Hong Yang:** Supervision, Writing – review & editing. **Jungang Hou:** Supervision, Writing – review & editing. **Chunshan Song:** Supervision, Writing – review & editing. **Xinwen Guo:** Conceptualization, Supervision, Writing – review & editing, Resources, Project administration.

Declaration of Competing Interest

The authors declare that they have no known competing financial interests or personal relationships that could have appeared to influence the work reported in this paper.

Data Availability

Data will be made available on request.

Acknowledgements

This work was financially supported by the National Natural Science Foundation of China (22278056), the Liaoning Revitalization Talent Program (XLYC2008032) and the Fundamental Research Funds for the Central Universities (DUT22LAB602). We thank J. Wang (from Dalian Institute of Chemical Physics) for advice on Mössbauer spectrometric analysis and D. Tian (from Dalian University of Technology) for DFT calculation help. VASP computation was performed on High Performance Computing facilities maintained by Information Technology Services at the University of Hong Kong.

Appendix A. Supporting information

Supplementary data associated with this article can be found in the online version at [doi:10.1016/j.apcatb.2023.122418](https://doi.org/10.1016/j.apcatb.2023.122418).

References

- [1] H. Rao, L.C. Schmidt, J. Bonin, M. Robert, Visible-light-driven methane formation from CO_2 with a molecular iron catalyst, *Nature* 548 (2017) 74–77.
- [2] M. Aresta, A. Dibenedetto, A. Angelini, Catalysis for the valorization of exhaust carbon: from CO_2 to chemicals, materials, and fuels. technological use of CO_2 , *Chem. Rev.* 114 (2014) 1709–1742.
- [3] J. Liang, Q. Wu, R. Cao, Reticular frameworks and their derived materials for CO_2 conversion by thermo-catalysis, *EnergyChem* 3 (2021), 100064.
- [4] Z. Fang, R. Ren, Y. Wang, Y. Hu, M. Dong, Z. Ye, Q. He, X. Peng, Solar-driven all-in-one MOFs-based catalyst for highly efficient CO_2 conversion, *Appl. Catal. B* 318 (2022), 121878.
- [5] J.A. Nathanael, K. Kannaiyan, A.K. Kunhiraman, S. Ramakrishna, V. Kumaravel, Global opportunities and challenges on net-zero CO_2 emissions towards a sustainable future, *React. Chem. Eng.* 6 (2021) 2226–2247.

- [6] H.L. Soest, M.G.J. Elzen, D.P. Vuuren, Net-zero emission targets for major emitting countries consistent with the paris agreement, *Nat. Commun.* 12 (2021) 2140.
- [7] J.L. White, M.F. Baruch, J.E. Pander III, Y. Hu, I.C. Fortmeyer, J.E. Park, T. Zhang, K. Liao, J. Gu, Y. Yan, Light-driven heterogeneous reduction of carbon dioxide: photocatalysts and photoelectrodes, *Chem. Rev.* 115 (2015) 12888–12935.
- [8] S. Cestellos-Blanco, H. Zhang, J.M. Kim, Y. Shen, P. Yang, Photosynthetic semiconductor biohybrids for solar-driven biocatalysis, *Nat. Catal.* 3 (2020) 245–255.
- [9] Y. Chai, Y. Chen, J. Shen, M. Ni, B. Wang, D. Li, Z. Zhang, X. Wang, Distortion of the coordination structure and high symmetry of the crystal structure in In_4SnS_8 microflowers for enhancing visible-light photocatalytic CO_2 reduction, *ACS Catal.* 11 (2021) 11029–11039.
- [10] X. Wang, J. He, J. Li, G. Lu, F. Dong, T. Majima, M. Zhu, Immobilizing perovskite CsPbBr_3 nanocrystals on Black phosphorus nanosheets for boosting charge separation and photocatalytic CO_2 reduction, *Appl. Catal. B* 277 (2020), 119230.
- [11] Z. Guo, G. Chen, C. Cometto, B. Ma, H. Zhao, T. Groizard, L. Chen, H. Fan, W.-L. Man, S.-M. Yiu, Selectivity control of CO versus HCOO^- production in the visible-light-driven catalytic reduction of CO_2 with two cooperative metal sites, *Nat. Catal.* 2 (2019) 801–808.
- [12] H. Takeda, K. Koike, H. Inoue, O. Ishitani, Development of an efficient photocatalytic system for CO_2 reduction using Rhenium(I) complexes based on mechanistic studies, *J. Am. Chem. Soc.* 130 (2008) 2023–2031.
- [13] Z. Jiang, X. Xu, Y. Ma, H.S. Cho, D. Ding, C. Wang, J. Wu, P. Oleynikov, M. Jia, J. Cheng, Filling metal-organic framework mesopores with TiO_2 for CO_2 photoreduction, *Nature* 586 (2020) 549–554.
- [14] Y. Wu, L. Yan, Y. Yu, C. Jing, Photocatalytic CO_2 reduction to CH_4 on iron porphyrin supported on atomically thin defective titanium dioxide, *Catal. Sci. Technol.* 11 (2021) 6103–6111.
- [15] M. Akatsuka, Y. Kawaguchi, R. Itoh, A. Ozawa, M. Yamamoto, T. Tanabe, T. Yoshida, Preparation of Ga_2O_3 photocatalyst highly active for CO_2 reduction with water without cocatalyst, *Appl. Catal. B* 262 (2020), 118247.
- [16] A. Li, Q. Cao, G. Zhou, B.V. Schmidt, W. Zhu, X. Yuan, H. Huo, J. Gong, M. Antonietti, Three-phase photocatalysis for the enhanced selectivity and activity of CO_2 reduction on a hydrophobic surface, *Angew. Chem. Int. Ed.* 58 (2019) 14549–14555.
- [17] Y. Li, S. Wang, X.-s Wang, Y. He, Q. Wang, Y. Li, M. Li, G. Yang, J. Yi, H. Lin, Facile top-down strategy for direct metal atomization and coordination achieving a high turnover number in CO_2 photoreduction, *J. Am. Chem. Soc.* 142 (2020) 19259–19267.
- [18] Z. Wang, J. Yang, J. Cao, W. Chen, G. Wang, F. Liao, X. Zhou, F. Zhou, R. Li, Z.-Q. Yu, Room-temperature synthesis of single iron site by electrofiltration for photoreduction of CO_2 into tunable syngas, *ACS Nano* 14 (2020) 6164–6172.
- [19] Y. Yang, J. Wu, T. Xiao, Z. Tang, J. Shen, H. Li, Y. Zhou, Z. Zou, Urchin-like hierarchical $\text{CoZnAl-LDH/RGO/g-C}_3\text{N}_4$ hybrid as a Z-scheme photocatalyst for efficient and selective CO_2 reduction, *Appl. Catal. B* 255 (2019), 117771.
- [20] J. Li, H. Huang, W. Xue, K. Sun, S. Song, C. Wu, L. Nie, Y. Li, C. Liu, Y. Pan, Self-adaptive dual-metal-site pairs in metal-organic frameworks for selective CO_2 photoreduction to CH_4 , *Nat. Catal.* 4 (2021) 719–729.
- [21] M. Ding, R.W. Flaig, H.-L. Jiang, O.M. Yaghi, Carbon capture and conversion using metal-organic frameworks and MOF-based materials, *Chem. Soc. Rev.* 48 (2019) 2783–2828.
- [22] H.-Q. Xu, J. Hu, D. Wang, Z. Li, Q. Zhang, Y. Luo, S.-H. Yu, H.-L. Jiang, Visible-light photoreduction of CO_2 in a metal-organic framework: boosting electron-hole separation via electron trap states, *J. Am. Chem. Soc.* 137 (2015) 13440–13443.
- [23] S.-Y. Han, D.L. Pan, H. Chen, X.B. Bu, Y.X. Gao, H. Gao, Y. Tian, G.S. Li, G. Wang, S. L. Cao, A methylthio-functionalized-MOF photocatalyst with high performance for visible-light-driven H_2 evolution, *Angew. Chem. Int. Ed.* 57 (2018) 9864–9869.
- [24] Y. Pi, X. Feng, Y. Song, Z. Xu, Z. Li, W. Lin, Metal-organic frameworks integrate Cu photosensitizers and secondary building unit-supported Fe catalysts for photocatalytic hydrogen evolution, *J. Am. Chem. Soc.* 142 (2020) 10302–10307.
- [25] Q. Mu, W. Zhu, X. Li, C. Zhang, Y. Su, Y. Lian, P. Qi, Z. Deng, D. Zhang, S. Wang, Electrostatic charge transfer for boosting the photocatalytic CO_2 reduction on metal centers of 2D MOF/rGO heterostructure, *Appl. Catal. B* 262 (2020), 118144.
- [26] H. Furukawa, K.E. Cordova, M. O’Keeffe, O.M. Yaghi, The chemistry and applications of metal-organic frameworks, *Science* 341 (2013) 1230444.
- [27] N. Li, J. Liu, J.J. Liu, L.Z. Dong, Z.F. Xin, Y.L. Teng, Y.Q. Lan, Adenine components in biomimetic metal-organic frameworks for efficient CO_2 photoconversion, *Angew. Chem. Int. Ed.* 58 (2019) 5226–5231.
- [28] J.D. Yi, R. Xie, Z.L. Xie, G.L. Chai, T.F. Liu, R.P. Chen, Y.B. Huang, R. Cao, Highly selective CO_2 electroreduction to CH_4 by in situ generated Cu_2O single-type sites on a conductive MOF: stabilizing key intermediates with hydrogen bonding, *Angew. Chem. Int. Ed.* 59 (2020) 23641–23648.
- [29] J.-D. Yi, R. Xu, Q. Wu, T. Zhang, K.-T. Zang, J. Luo, Y.-L. Liang, Y.-B. Huang, R. Cao, Atomically dispersed iron-nitrogen active sites within porphyrinic triazine-based frameworks for oxygen reduction reaction in both alkaline and acidic media, *ACS Energy Lett.* 3 (2018) 883–889.
- [30] C. He, Q.-J. Wu, M.-J. Mao, Y.-H. Zou, B.-T. Liu, Y.-B. Huang, R. Cao, Multifunctional gold nanoparticles@imidazolium-based cationic triazine frameworks for efficient tandem reactions, *CCS Chem.* 3 (2021) 2368–2380.
- [31] T. Kong, Y. Jiang, Y. Xiong, Photocatalytic CO_2 conversion: what can we learn from conventional CO_x hydrogenation? *Chem. Soc. Rev.* 49 (2020) 6579–6591.
- [32] X. Chang, T. Wang, J. Gong, CO_2 photo-reduction: insights into CO_2 activation and reaction on surfaces of photocatalysts, *Energy Environ. Sci.* 9 (2016) 2177–2196.
- [33] Y. Fu, D. Sun, Y. Chen, R. Huang, Z. Ding, X. Fu, Z. Li, An amine-functionalized titanium metal-organic framework photocatalyst with visible-light-induced activity for CO_2 reduction, *Angew. Chem. Int. Ed.* 51 (2012) 3364–3367.
- [34] X.-P. Wu, L. Gagliardi, D.G. Truhlar, Cerium metal-organic framework for photocatalysis, *J. Am. Chem. Soc.* 140 (2018) 7904–7912.
- [35] B. Pattengale, S. Yang, J. Ludwig, Z. Huang, X. Zhang, J. Huang, Exceptionally long-lived charge separated state in zeolitic imidazolate framework: implication for photocatalytic applications, *J. Am. Chem. Soc.* 138 (2016) 8072–8075.
- [36] E.M. Mahmoud, H. Audi, A. Assoud, T.H. Ghaddar, M. Hmadeh, Metal-organic framework photocatalyst incorporating bis(4'-(4-carboxyphenyl)-terpyridine) ruthenium(II) for visible-light-driven carbon dioxide reduction, *J. Am. Chem. Soc.* 141 (2019) 7115–7121.
- [37] P.M. Stanley, C. Thomas, E. Thyrhaug, A. Urstoeger, M. Schuster, Jr Hauer, B. Rieger, J. Warnan, R.A. Fischer, Entrapped molecular photocatalyst and photosensitizer in metal-organic framework nanoreactors for enhanced solar CO_2 reduction, *ACS Catal.* 11 (2021) 871–882.
- [38] J. Ge, Y. Sun, W. Chen, F. Song, Y. Xie, Y. Zheng, P. Rao, Z-scheme heterojunction based on $\text{NiWO}_4/\text{WO}_3$ microspheres with enhanced photocatalytic performance under visible light, *Dalton Trans.* 50 (2021) 13801–13814.
- [39] C. Wang, M. Cai, Y. Liu, F. Yang, H. Zhang, J. Liu, S. Li, Facile construction of novel organic-inorganic tetra (4-carboxyphenyl) porphyrin/ Bi_2MoO_6 heterojunction for tetracycline degradation: Performance, degradation pathways, intermediate toxicity analysis and mechanism insight, *J. Colloid Interface Sci.* 605 (2022) 727–740.
- [40] Z. Fang, B. Bueken, D.E. De Vos, R.A. Fischer, Defect-engineered metal-organic frameworks, *Angew. Chem. Int. Ed.* 54 (2015) 7234–7254.
- [41] C. Xu, Y. Pan, G. Wan, H. Liu, L. Wang, H. Zhou, S.-H. Yu, H.-L. Jiang, Turning on visible-light photocatalytic C-H oxidation over metal-organic frameworks by introducing metal-to-cluster charge transfer, *J. Am. Chem. Soc.* 141 (2019) 19110–19117.
- [42] C. He, J. Liang, Y.-H. Zou, J.-D. Yi, Y.-B. Huang, R. Cao, Metal-organic frameworks bonded with metal N-heterocyclic carbenes for efficient catalysis, *Natl. Sci. Rev.* 9 (2022) nwab157.
- [43] E.X. Chen, M. Qiu, Y.F. Zhang, Y.S. Zhu, L.Y. Liu, Y.Y. Sun, X. Bu, J. Zhang, Q. Lin, Acid and base resistant zirconium polyphenolate-metalloporphyrin scaffolds for efficient CO_2 photoreduction, *Adv. Mater.* 30 (2018) 1704388.
- [44] G. Kresse, J. Furthmüller, Efficient iterative schemes for ab initio total-energy calculations using a plane-wave basis set, *Phys. Rev. B* 54 (1996) 11169–11186.
- [45] P.E. Blöchl, Projector augmented-wave method, *Phys. Rev. B* 50 (1994) 17953–17979.
- [46] G. Kresse, D. Joubert, From ultrasoft pseudopotentials to the projector augmented-wave method, *Phys. Rev. B* 59 (1999) 1758–1775.
- [47] H. Peng, I.G. McKendry, R. Ding, A.C. Thenuwara, Q. Kang, S.L. Shumlas, D. R. Strongin, M.J. Zdzila, J.P. Perdew, Redox properties of birnessite from a defect perspective, *Proc. Nat. Acad. Sci.* 114 (2017) 9523–9528.
- [48] M. Capdevila-Cortada, Z. Łodziana, N. López, Performance of DFT+U approaches in the study of catalytic materials, *ACS Catal.* 6 (2016) 8370–8379.
- [49] S. Grimme, J. Antony, S. Ehrlich, H. Krieg, A consistent and accurate ab initio parametrization of density functional dispersion correction (DFT-D) for the 94 elements H-Pu, *J. Chem. Phys.* 132 (2010), 154104.
- [50] A.D. Becke, Density-functional thermochemistry. I. The effect of the exchange-only gradient correction, *J. Chem. Phys.* 96 (1992) 2155–2160.
- [51] A. Schäfer, H. Horn, R. Ahlrichs, Fully optimized contracted gaussian basis sets for atoms Li to Kr, *J. Chem. Phys.* 97 (1992) 2571–2577.
- [52] M.J. Frisch, G.W. Trucks, H.B. Schlegel, G.E. Scuseria, M.A. Robb, J.R. Cheeseman, G. Scalmani, V. Barone, G.A. Petersson, H. Nakatsuji, X. Li, M. Caricato, A.V. Marenich, J. Bloino, B.G. Janesko, R. Gomperts, B. Mennucci, H.P. Hratchian, J.V. Ortiz, A.F. Izmaylov, J.L. Sonnenberg, Williams, F. Ding, F. Lipparini, F. Egidi, J. Goings, B. Peng, A. Petrone, T. Henderson, D. Ranasinghe, V.G. Zakrzewski, J. Gao, N. Rega, G. Zheng, W. Liang, M. Hada, M. Ehara, K. Toyota, R. Fukuda, J. Hasegawa, M. Ishida, T. Nakajima, Y. Honda, O. Kitao, H. Nakai, T. Vreven, K. Throssell, J.A. Montgomery Jr, J.E. Peralta, F. Ogliaro, M.J. Bearpark, J.J. Heyd, E. N. Brothers, K.N. Kudin, V.N. Staroverov, T.A. Keith, R. Kobayashi, J. Normand, K. Raghavachari, A.P. Rendell, J.C. Burant, S.S. Iyengar, J. Tomasi, M. Cossi, J.M. Millam, M. Klene, C. Adamo, R. Cammi, J.W. Ochterski, R.L. Martin, K. Morokuma, O. Farkas, J.B. Foresman, D.J. Fox, *Gaussian 16 Rev. C.01*, Wallingford, CT, 2016.
- [53] H.L. Nguyen, F. Gándara, H. Furukawa, T.L. Doan, K.E. Cordova, O.M. Yaghi, A titanium-organic framework as an exemplar of combining the chemistry of metal- and covalent-organic frameworks, *J. Am. Chem. Soc.* 138 (2016) 4330–4333.
- [54] S. An, G. Zhang, T. Wang, W. Zhang, K. Li, C. Song, J.T. Miller, S. Miao, J. Wang, X. Guo, High-density ultra-small clusters and single-atom Fe sites embedded in graphitic carbon nitride (g- C_3N_4) for highly efficient catalytic advanced oxidation processes, *ACS Nano* 12 (2018) 9441–9450.
- [55] D. Sun, Y. Fu, W. Liu, L. Ye, D. Wang, L. Yang, X. Fu, Z. Li, Studies on photocatalytic CO_2 reduction over $\text{NH}_2\text{-UiO-66(Zr)}$ and its derivatives: towards a better understanding of photocatalysis on metal-organic frameworks, *Chem. Eur. J.* 19 (2013) 14279–14285.
- [56] L. Li, S. Zhang, L. Xu, J. Wang, L.-X. Shi, Z.-N. Chen, M. Hong, J. Luo, Effective visible-light driven CO_2 photoreduction via a promising bifunctional iridium coordination polymer, *Chem. Sci.* 5 (2014) 3808–3813.
- [57] D. Sun, W. Liu, M. Qiu, Y. Zhang, Z. Li, Introduction of a mediator for enhancing photocatalytic performance via post-synthetic metal exchange in metal-organic frameworks (MOFs), *Chem. Commun.* 51 (2015) 2056–2059.
- [58] X.-X. Li, J. Liu, L. Zhang, L.-Z. Dong, Z.-F. Xin, S.-L. Li, X.-Q. Huang-Fu, K. Huang, Y.-Q. Lan, Hydrophobic polyoxometalate-based metal-organic framework for efficient CO_2 photoconversion, *ACS Appl. Mater. Interfaces* 11 (2019) 25790–25795.

- [59] Y. Lee, S. Kim, J. Kang, S.M. Cohen, Photocatalytic CO₂ reduction by a mixed metal (Zr/Ti), mixed ligand metal-organic framework under visible light irradiation, *Chem. Commun.* 51 (2015) 5735–5738.
- [60] D. Wang, R. Huang, W. Liu, D. Sun, Z. Li, Fe-based MOFs for photocatalytic CO₂ reduction: role of coordination unsaturated sites and dual excitation pathways, *ACS Catal.* 4 (2014) 4254–4260.
- [61] D. Sun, Y. Gao, J. Fu, X. Zeng, Z. Chen, Z. Li, Construction of a supported Ru complex on bifunctional MOF-253 for photocatalytic CO₂ reduction under visible light, *Chem. Commun.* 51 (2015) 2645–2648.
- [62] T.-C. Zhuo, Y. Song, G.-L. Zhuang, L.-P. Chang, S. Yao, W. Zhang, Y. Wang, P. Wang, W. Lin, T.-B. Lu, H-bond-mediated selectivity control of formate versus CO during CO₂ photoreduction with two cooperative Cu/X sites, *J. Am. Chem. Soc.* 143 (2021) 6114–6122.
- [63] Z.-H. Yan, M.-H. Du, J. Liu, S. Jin, C. Wang, G.-L. Zhuang, X.-J. Kong, L.-S. Long, L.-S. Zheng, Photo-generated dinuclear {Eu(II)}₂ active sites for selective CO₂ reduction in a photosensitizing metal-organic framework, *Nat. Commun.* 9 (2018) 3353.
- [64] Y.-C. Hao, L.-W. Chen, J. Li, Y. Guo, X. Su, M. Shu, Q. Zhang, W.-Y. Gao, S. Li, Z.-L. Yu, Metal-organic framework membranes with single-atomic centers for photocatalytic CO₂ and O₂ reduction, *Nat. Commun.* 12 (2021) 2682.
- [65] M. Sun, S. Yan, Y. Sun, X. Yang, Z. Guo, J. Du, D. Chen, P. Chen, H. Xing, Enhancement of visible-light-driven CO₂ reduction performance using an amine-functionalized zirconium metal-organic framework, *Dalton Trans.* 47 (2018) 909–915.
- [66] Y.-N. Gong, W. Zhong, Y. Li, Y. Qiu, L. Zheng, J. Jiang, H.-L. Jiang, Regulating photocatalysis by spin-state manipulation of cobalt in covalent organic frameworks, *J. Am. Chem. Soc.* 142 (2020) 16723–16731.
- [67] K. Guo, X. Zhu, L. Peng, Y. Fu, R. Ma, X. Lu, F. Zhang, W. Zhu, M. Fan, Boosting photocatalytic CO₂ reduction over a covalent organic framework decorated with ruthenium nanoparticles, *Chem. Eng. J.* 405 (2021), 127011.
- [68] M. Lu, Q. Li, J. Liu, F.-M. Zhang, L. Zhang, J.-L. Wang, Z.-H. Kang, Y.-Q. Lan, Installing earth-abundant metal active centers to covalent organic frameworks for efficient heterogeneous photocatalytic CO₂ reduction, *Appl. Catal. B* 254 (2019) 624–633.
- [69] R. Kuriki, O. Ishitani, K. Maeda, Unique solvent effects on visible-light CO₂ reduction over ruthenium(II)-complex/carbon nitride hybrid photocatalysts, *ACS Appl. Mater. Interfaces* 8 (2016) 6011–6018.
- [70] F. Yoshitomi, K. Sekizawa, K. Maeda, O. Ishitani, Selective formic acid production via CO₂ reduction with visible light using a hybrid of a perovskite tantalum oxynitride and a binuclear ruthenium(II) complex, *ACS Appl. Mater. Interfaces* 7 (2015) 13092–13097.
- [71] S. Sato, T. Morikawa, S. Saeki, T. Kajino, T. Motohiro, Visible-light-induced selective CO₂ reduction utilizing a ruthenium complex electrocatalyst linked to ap-type nitrogen-doped Ta₂O₅ semiconductor, *Angew. Chem. Int. Ed.* 49 (2010) 5101–5105.
- [72] T. Baran, S. Wojtyła, A. Dibenedetto, M. Aresta, W. Macyk, Zinc sulfide functionalized with ruthenium nanoparticles for photocatalytic reduction of CO₂, *Appl. Catal. B* 178 (2015) 170–176.
- [73] D. An, S. Nishioka, S. Yasuda, T. Kanazawa, Y. Kamakura, T. Yokoi, S. Nozawa, K. Maeda, Alumina-supported alpha-iron(III) oxyhydroxide as a recyclable solid catalyst for CO₂ photoreduction under visible light, *Angew. Chem. Int. Ed.* 62 (2022), e202204948.
- [74] S.-J. Yao, N. Li, J. Liu, L.-Z. Dong, J.-J. Liu, Z.-F. Xin, D.-S. Li, S.-L. Li, Y.-Q. Lan, Ferrocene-functionalized crystalline biomimetic catalysts for efficient CO₂ photoreduction, *Inorg. Chem.* 61 (2022) 2167–2173.
- [75] Q. Zhu, Y. Cao, Y. Tao, T. Li, Y. Zhang, H. Shang, J. Song, G. Li, CO₂ reduction to formic acid via NH₂-C@Cu₂O photocatalyst in situ derived from amino modified Cu-MOF, *J. CO₂ UTIL* 54 (2021), 101781.
- [76] T.M. Suzuki, T. Takayama, S. Sato, A. Iwase, A. Kudo, T. Morikawa, Enhancement of CO₂ reduction activity under visible light irradiation over Zn-based metal sulfides by combination with Ru-complex catalysts, *Appl. Catal. B* 224 (2018) 572–578.
- [77] S. Guo, L.-H. Kong, P. Wang, S. Yao, T.-B. Lu, Z.-M. Zhang, Switching excited state distribution of metal-organic framework for dramatically boosting photocatalysis, *Angew. Chem. Int. Ed.* 61 (2022), e202206193.
- [78] N. Sadeghi, S. Sharifnia, T.-O. Do, Enhanced CO₂ photoreduction by a graphene-porphyrin metal-organic framework under visible light irradiation, *J. Mater. Chem. A* 6 (2018) 18031–18035.
- [79] K. Mori, J. Matsuo, Y. Kondo, H. Hata, H. Yamashita, Photoreduction of carbon dioxide to formic acid with Fe-based MOFs: the promotional effects of heteroatom doping and alloy nanoparticle confinement, *ACS Appl. Energy Mater.* 4 (2021) 11634–11642.
- [80] F.M. Wissler, M. Duguet, Q. Perrinet, A.C. Ghosh, M. Alves-Favaro, Y. Mohr, C. Lorentz, E.A. Quadrelli, R. Palkovits, D. Farrusseng, Molecular porous photosystems tailored for long-term photocatalytic CO₂ reduction, *Angew. Chem. Int. Ed.* 59 (2020) 5116–5122.
- [81] E.I. Solomon, T.C. Brunold, M.I. Davis, J.N. Kemsley, S.-K. Lee, N. Lehnert, F. Neese, A.J. Skulan, Y.-S. Yang, J. Zhou, Geometric and electronic structure/function correlations in non-heme iron enzymes, *Chem. Rev.* 100 (2000) 235–350.
- [82] S. Shoji, X. Peng, A. Yamaguchi, R. Watanabe, C. Fukuhara, Y. Cho, T. Yamamoto, S. Matsumura, M.-W. Yu, S. Ishii, Photocatalytic uphill conversion of natural gas beyond the limitation of thermal reaction systems, *Nat. Catal.* 3 (2020) 148–153.
- [83] X. Li, J. Yu, M. Jaroniec, X. Chen, Cocatalysts for selective photoreduction of CO₂ into solar fuels, *Chem. Rev.* 119 (2019) 3962–4179.
- [84] J. Albero, Y. Peng, H. García, Photocatalytic CO₂ reduction to C₂+ products, *ACS Catal.* 10 (2020) 5734–5749.
- [85] M. Gutierrez, B. Cohen, F. Sánchez, A. Douhal, Photochemistry of Zr-based MOFs: ligand-to-cluster charge transfer, energy transfer and excimer formation, what else is there? *Phys. Chem. Chem. Phys.* 18 (2016) 27761–27774.
- [86] H. Zhang, J. Wei, J. Dong, G. Liu, L. Shi, P. An, G. Zhao, J. Kong, X. Wang, X. Meng, Efficient visible-light-driven carbon dioxide reduction by a single-atom implanted metal-organic framework, *Angew. Chem. Int. Ed.* 55 (2016) 14310–14314.
- [87] I.V. Chernyshova, P. Somasundaran, S. Ponnurangam, On the origin of the elusive first intermediate of CO₂ electroreduction, *PNAS* 115 (2018) E9261–E9270.
- [88] H. Liu, Y. Su, S. Kuang, E.J. Hensen, S. Zhang, X. Ma, Highly efficient CO₂ electrolysis within a wide operation window using octahedral tin oxide single crystals, *J. Mater. Chem. A* 9 (2021) 7848–7856.
- [89] S. Yuan, L. Feng, K. Wang, J. Pang, M. Bosch, C. Lollar, Y. Sun, J. Qin, X. Yang, P. Zhang, Stable metal-organic frameworks: design, synthesis, and applications, *Adv. Mater.* 30 (2018) 1704303.